

Seismic velocity estimation using passive downhole distributed acoustic sensing records - examples from the San Andreas Fault Observatory at Depth

Ariel Lellouch, Siyuan Yuan, Zack Spica, Biondo Biondi, and William L. Ellsworth

ABSTRACT

^a Structural imaging and event localization require an accurate estimation of the seismic velocity. However, active seismic surveys are expensive and time-consuming. During the last decade, fiber-optic-based distributed acoustic sensing (DAS) has emerged as a reliable, enduring, and high-resolution seismic sensing technology. In this study, we show how downhole DAS passive records from the San Andreas Fault Observatory at Depth can be used for seismic velocity estimation. Using data recorded from earthquakes propagating near-vertically, we compute seismic velocities using first-break picking as well as slant-stack decomposition. This methodology allows for the estimation of both P- and S- wave velocity models. We also use records of the ambient seismic field for interferometry and P-wave velocity model extraction. Results are compared to a regional model obtained from surface seismic as well as a conventional downhole geophone survey. We find that using recorded earthquakes we obtain the highest P-wave model resolution. In addition, it is the only method that allows for S-wave velocity estimation. Obtained P and S models unravel three distinct layers at the depth range of 50-750 m which were not present in the regional model. In addition, we find high V_P/V_S values near the surface and a possible V_P/V_S anomaly about 500 m deep. We confirm its existence by observing a strong S-P mode conversion at that depth.

^aThe following is a minor variation of a JGR: Solid Earth submission

INTRODUCTION

An accurate estimation of the seismic velocity profile is crucial for structural imaging and its ensuing interpretation. It is also important for earthquake location, even though reliable relative locations between clusters of events may be obtained without an accurate model (Waldhauser and Ellsworth, 2000). In conventional processing, retrieving the velocity field above the bedrock is usually a major obstacle (Bakulin and Calvert, 2006). This challenge is due, among others, to a lack of reflection events above the bedrock, velocity variation with depth due to compaction, inhomogeneity in all spatial directions, and the presence of scatterers. Errors in estimating the shallow

subsurface velocity deteriorates the image quality of deeper targets (Armstrong et al., 2001; Blias, 2009; Nosjean et al., 2017).

Using downhole measurements can help alleviate some of the difficulties in shallow subsurface velocity estimation (Bakulin et al., 2017). The most widespread method is the vertical seismic profiling (VSP), in which a source is excited at the surface and recorded at different depth levels along the well (Hardage, 2000). Nonetheless, conducting VSP surveys is challenging as it requires the lowering and clamping of receivers, usually geophones, into a borehole before exciting the source. Such receivers have to withstand harsh temperature and pressure conditions, depending on their depth of installation. In addition, other operations in the borehole are limited during the VSP survey, and such measurements cannot be conducted in a hydrocarbon-producing well. An enticing alternative is the emerging technology of distributed acoustic sensing (DAS). DAS utilizes a fiber-optic cable instead of geophones for seismic sensing along the well (Mateeva et al., 2013). The fiber is probed by a laser interrogator that measures deformation along the fiber due to its interaction with seismic waves. A more detailed description of its operating principles is discussed in the DAS recording system section. Fibers can be installed in several different ways that do not interfere with the well (Daley et al., 2013). As the fiber is a passive component, no electronic equipment needs to be lowered down into the borehole and fibers may be left in the ground for a virtually unlimited amount of time.

In this study, we show how downhole passive DAS records can be used for velocity model estimation. We use earthquakes propagating near-vertically and recorded by a DAS downhole array to build P and S velocity models at the borehole location. Relatively weak recorded earthquakes have a high frequency content, which allows for high-resolution model estimation. In contrary to conventional VSP surveys, this approach does not require a dedicated survey, can be used to directly extract S-velocity profiles, is within the far-field limit, and can be repeated at different times at almost no additional cost. In addition, we show an ambient seismic field interferometry approach, yielding a P-wave velocity model. To our knowledge, this is the first application of interferometry to downhole DAS records. It can be especially helpful in seismically quiet areas. We illustrate the application of both methods using the San Andreas Fault Observatory at Depth (SAFOD) main hole, in which a fiber is installed. We compare our suggested approach to a conventional VSP experiment conducted with downhole geophones and a regional model of the area.

EXPERIMENTAL SETUP

The DAS recording system

During the recent years, DAS has been proven apt at recording seismic data at a high spatial resolution. It has been used for both active surveys and passive monitoring, onshore and offshore, and as a downhole as well as a horizontally installed sensor (Ajo-

Franklin et al., 2017; Biondi et al., 2017; Daley et al., 2013, 2016; Dou et al., 2017; Hornman, 2017; Jousset et al., 2018; Karrenbach et al., 2017; Lindsey et al., 2017; Martin et al., 2017a,b; Martin and Biondi, 2018; Mateeva et al., 2014, 2013; Wang et al., 2018). DAS systems are commonly based on Rayleigh backscattering of a laser pulse propagating through an optical fiber. Due to imperfections in the fiber, some of the propagating energy is reflected back during propagation. When the fiber is idle, such backscattering is constant. On the contrary, when the fiber is distorted due to an interaction with a seismic wave, some photons are reflected in a different way. An interrogator unit, connected to one end of the fiber, continuously sends short laser pulses through the fiber. Recorded reflected photons undergo interferometry with the reference transmitted pulse and the resulting phase shift is quasi-linearly proportional to total strain along the direction of the fiber (Grattan and Meggitt, 2000).

In its simplest form, DAS acts as a strain meter. However, as there is no single DAS architecture, systems operating in time or frequency domain may measure either strain or strain-rate, accordingly. The acquisition setup used for this study measures strain with respect to a certain baseline reference, which is the natural backscattering of the fiber. As the speed of light in the fiber is known, the time of arrival of the backscattered energy can be mapped to the distance along the fiber (Parker et al., 2014). By repeating the phase-shift measurement during the pulse propagation time, one can actually compute strain variations in different sections of the fiber. By differentiating these cumulative strain measurements, acquired at different times during pulse propagation, a spatially-dependent strain profile may then be obtained. This is the distributed nature of the measurement. If subsequent pulses are generated quickly enough, a strain profile along the fiber can be determined at acoustic frequencies. DAS systems are single-component and measure strain or strain-rate along the fiber. Therefore, directivity effects depending on source radiation pattern, mode of propagating wavefronts, and fiber orientation, are visible in recorded signals (Martin, 2018). In our analysis, we convert strain records to strain-rate by taking their derivative in time. This removes the dependency on the natural backscattering of the fiber, which is constant in time.

There are many more technical details about DAS systems and their comparison to standard instruments (e.g. Grattan and Meggitt (2000)). For our purposes, we describe only the gauge length, which is the length over which the phase shifts are measured. It effectively acts as a moving window spatially averaging strain. A detailed explanation of gauge length effects is given by Dean et al. (2017). In short, longer gauge lengths promote higher SNR while filtering out high-frequency components of the data. In this study, a standard 10m gauge length was used for data acquisition. It is adequate for typical 0-100 Hz recorded events, such as the ones we examine.

The SAFOD DAS array

A detailed description of the SAFOD experiment can be found in Zoback et al. (2011). In June 2017, an OptaSense DAS interrogator, model ODH3.1, was attached to the longer fiber in the SAFOD main hole, reaching a depth of 864m. Due to a failure of the loop at the end of the fiber, we limit our analysis to a depth of 800m. The reason for that choice is that starting approximately at the failure depth, the records contain no signal at all. However, in the depth range of 800m to the failure depth, the records seem to contain many more noise channels. While some of the channels can be used, we suspect that they might be corrected in some way and thus choose not to use them. The fibers are under tension of approximately 1N and housed in a 0.9 mm steel tube cemented between casing strings. We illustrate the area of the well that is covered by our analysis in Figure 1. In the depth range of interest, the well is deviating north. For comparison, we later show the analysis of a geophone survey conducted during 2005 in the same well. Geophones were located roughly every 15m, starting at a depth of 45m, and the two explosive sources were more than 40m away from the wellhead. The goal of that survey was to assess the SAFOD main hole. Since the DAS was deployed in the same well, we can compare the two results.

It is important to note that the DAS interrogator can map strain as a function of distance along the fiber. However, distance along the fiber is not necessarily equal to distance along the well. Mapping fiber distance to spatial coordinates is not trivial (Mateeva et al., 2014) and might require advanced calibration procedures if a simple stretch mapping using two reference points cannot be computed. For the SAFOD array, the fiber, a single mode type (model SMF28, see Blum et al. (2008) for details), was put in a steel tube and under tension, and therefore its length is expected to match the location along the well. However, minor discrepancies may arise due to fiber slack, rotation, and by-design excess fiber length (Madsen et al., 2016). As the initial installation of the fiber was conducted over a decade ago, it is also possible that the fiber underwent environment-based changes affecting its installation or internal properties. As a side note, it is worth mentioning that the same fiber can also be used as a permanent strain meter, measuring fault-induced displacements. Since a long baseline strain recording of SAFOD was acquired, structural changes could be detected. However, this is not the focus of this study. The recording system was operative for about a month during June-July 2017. Due to technical issues, about 22 days of recorded data are useful. Data were recorded at a 2500 Hz frequency with a 10 m gauge length and a 1 m channel spacing. The interrogator used in this study measures strain along the fiber.

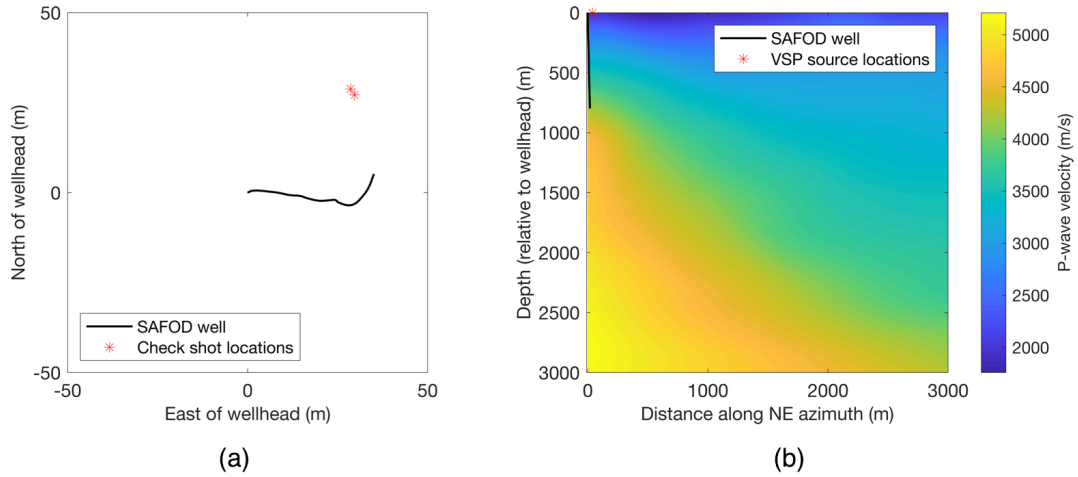


Figure 1: The SAFOD borehole in map (a) and side (b) view. The side view is along the NE azimuth, which is perpendicular to the San Andreas Fault. The well trajectory is plotted as a black line. Source locations for the geophone survey are plotted as red stars. A 2-D section crossing the fault zone and taken along the NE azimuth from a regional P-wave velocity model (Hole et al., 2006) is displayed in the background. [NR]

VELOCITY MODEL ESTIMATION USING EARTHQUAKES RECORDED BY DOWNHOLE DAS

Theory

In this section, we schematically describe a uniaxial downhole recording of an incident plane wave (Figure 2). The vertical axis denotes depth.

We approximate the propagating wavefield as plane wave recorded by receivers, idealized as a set of discrete points R_i at equal sampling distances, with n being the points index along the fiber. Assuming the distance between two adjacent measurement points is dz , the arrival time difference between them is, geometrically,

$$t_n - t_{n+1} = \frac{dz \cdot \cos \theta}{V} \quad (1)$$

with V being the wave propagation velocity in the medium, assumed to be constant. t_n is the time of arrival at receiver n . This relation can also be generalized for depth-dependent velocity V and varying incidence angle θ . It becomes a locally correct approximation within a region in which the propagating wave can be regarded as a planar one. Nonetheless, the angle of incidence is unknown to us in the general case, and it is impossible to separate subsurface velocity from the incidence angle even if arrival travel times are correctly estimated.

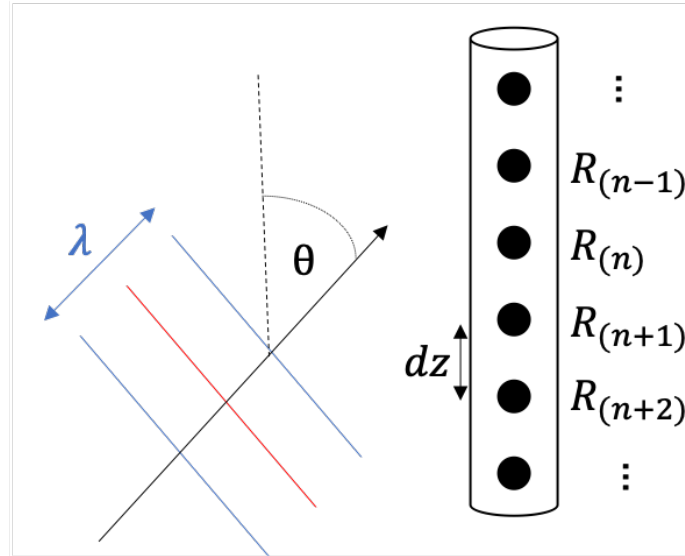


Figure 2: Schematic representation of a planar wave-front reaching a discrete down-hole array. The distance between receivers, denoted as black circles, is dz . The angle θ marks the angle between the direction of propagation (Poynting vector) and the array, represented by discrete receivers R_i . The wavelength λ is schematically indicated. **[NR]**

However, using events located directly above or below the DAS array, propagation is guaranteed to be along the direction of the vertical well assuming no lateral velocity variation. In this case, the angle of incidence is always $\theta = 0^\circ$ or 180° , and we can compute the average velocity V_n in the interval between the two receivers $[R_n, R_{n+1}]$ by

$$V_i = \frac{dz}{|t_n - t_{n+1}|} \quad (2)$$

This relation holds at every location along the fiber and may thus be used for continuous estimation of the velocity profile $V(z)$ along it.

In DAS records, strain (or strain-rate) is measured along the fiber, which in this study is near-vertical and assumed as vertical. Transforming a point strain measurement to an equivalent conventional geophone, measuring ground velocity along the vertical direction, is based on the following relation:

$$\frac{\partial u_z}{\partial z} = \frac{\partial u_z}{\partial t} \cdot \frac{\partial t}{\partial z} = \frac{\partial u_z}{\partial t} \cdot \frac{1}{v} \quad (3)$$

where u_z is the particle displacement in the z -direction and $1/v$ is the local apparent slowness. This slowness depends on both subsurface velocity model v and the

wavefronts angle of incidence. While the $1/v$ scaling may influence the amplitude of recorded data, it does not change its phase. Therefore, any travel-times based analysis, using earthquakes or the ambient seismic field, should yield the same result for both DAS and geophone-equivalent data. In addition, DAS is not a point measurement and gauge length effects may affect phase by distorting wavelets (Dean et al., 2017). However, as previously stated, the gauge length is adequate for recorded events of interest and we do not observe any noticeable wavelet distortion. In this study, we compute strain-rate by applying a time derivative to recorded strain data. Since the subsurface velocity v (Equation 3) is constant with respect to time, this amounts to using accelerometer-equivalent data, and the scaling relations remain the same.

DAS systems have two major benefits in terms of velocity model estimation. Their spatial density allows for high-resolution models and the fiber installation is permanent. In this study, we suggest using earthquakes recorded by DAS arrays for velocity model estimation. Such earthquakes have to fulfill two major criteria. First, they have to induce strain that is measurable by the vertical DAS array with high signal-to-noise ratio. This is a function of source moment, focal mechanism, and distance from the array. Second, they have to reach the array in a near-vertical incidence angle. Since the velocity model between the source and the array also influences the direction of propagation, it is not enough to know the source location to compute the angle of incidence. However, as a rule of thumb, a 15- to 20-degree angle, computed using straight lines, is acceptable. This is thanks to the overall trend of velocity increase with depth, which bends propagating wave-fronts towards the vertical incidence. Assuming such earthquakes are present, this approach does not require the deployment of a source, can be repeated for different adequate earthquakes, and does not suffer from the near-field limitations often present in VSP surveys due to proximity of the source to the recording array (Landrø, 1999). In addition, since only differential travel times are used, the source origin time is irrelevant and does not need to be known.

An ideal earthquake for velocity estimation would be located directly below the array. As such, primary phase wave-propagation is 1-D and Equation (2) can be directly applied. However, many other earthquakes may still be used. First, the correction term depending on the angle of incidence θ is proportional to $1/\cos \theta$. A local incidence angle of 10 degrees induces about 1.5% increase in the estimated velocity. This effect may also be corrected by computing the local incidence angle (θ_{est}) at each receiver using some initial structural model of the area and correcting the estimated interval velocity by a $\cos \theta_{est}$ factor. Having said that, such corrections may often be omitted due to real-world velocity structures. In this study, for example, earthquakes originate at far larger depths than the recording array. As velocity is generally increasing with depth, the shortest trajectory from source to receiver will bend towards a vertical path, following Snells law. Therefore, the true incidence angle will be closer to zero (vertical incidence) than its angle computed by a straight line from receiver to source.

Recorded earthquakes

For this study, we observe two earthquakes recorded by the array. Both were chosen using the USGS catalog in that area. Using event timing, relevant DAS data was extracted. The first event is a magnitude $M=1.33$, located at a depth of $Z=11.16$ km and at a horizontal distance of $H=1.87$ km from the wellhead. The second is $M = 2.46$ km located at $Z = 11.43$ km and $H = 2.49$ km. For a uniform half-space, their angles of incidence at the bottom of the array would be about 10.2° and 13.2° , respectively. Since they are located at great depths, at which velocity is higher, we expect significant ray bending. A regional model of the area (Hole et al., 2006; Bleibinhaus et al., 2007) estimates P-wave velocity along the array at about 2500 m/s (close to the surface) to 4000 m/s (bottom of the array). Velocities of 6000 m/s are observed at depths of 5 – 6 km, and it can be expected up to the depth of the earthquakes. Therefore, even using a conservative correction, the angles of incidence would be 6.8° and 8.7° . This amount to an average $< 1\%$ correction of the velocity at the bottom of the array, which is where the incidence angle has the highest impact. Due to velocity increase with depth along the array, the effect would be smaller as we get closer to the surface. Overall, having shown that the error can be safely bounded by an average 1% over-estimation of the velocity, we will treat recorded events as vertical.

In Figure 3, we show recorded earthquakes. Noisy traces are automatically detected and set to zero amplitude. We also apply a trace-by-trace normalization to enhance events. The $M = 1.33$ is in (a) and the $M = 2.46$ in (b). The same ordering will follow for the rest of the paper. Notable events are marked in the figure. Notice also the signal-to-noise and frequency range differences between the two earthquakes. The larger $M = 2.46$ earthquake (b) has lower frequency content, visible especially in the first arrival P-waves. It also has a higher signal-to-noise ratio, as can be seen by the level of noise preceding the first arrivals. Due to technical issues with file headers for the earthquake in (b), absolute time is only approximated. However, the two events seem to have similar behavior and arrival moveouts. For all subsequent velocity estimation purposes, only the $M = 1.33$ event is used. The reason is that for the $M = 2.46$ event, we could not coherently follow the first S-wave arrivals. Since we want a fair comparison between different methods, we chose to base our analysis on a single event for all of them. In addition, the central frequency of the $M = 1.33$ event is around 70 Hz. The $M = 2.46$ has, as expected, a lower frequency content, thus we prefer to use the weaker earthquake for the benefit of increased temporal resolution at the price of lower signal-to-noise.

Estimating velocity by travel-time picking

We begin by estimating the P-wave velocity along the array. The first arrival phase is picked for both earthquakes. It is conducted using a linear programming approach, aiming at maximizing total energy along a picking path. However, many other choices

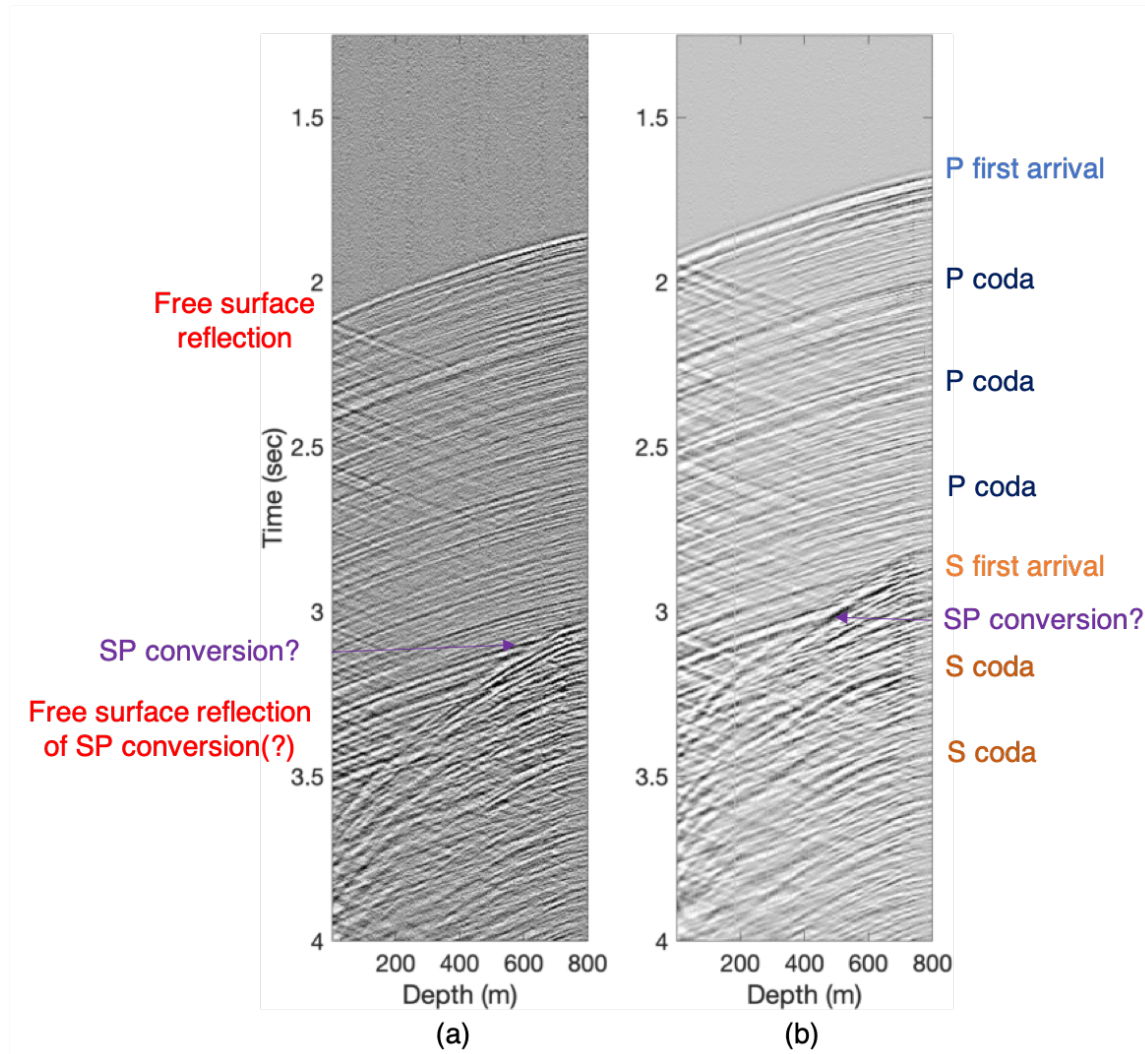


Figure 3: Earthquakes recorded in SAFOD DAS array, filtered in the 0 – 120 Hz range. $M = 1.33$ (a) and $M = 2.46$ (b) events are plotted. Many different phases are present, some of which are indicated by text alongside the seismograms. Unless an arrow is present, the text matches the time of arrival of the event. In addition to direct P and S arrivals, we clearly observe P and S coda events, possible SP conversions, and free surface reflections of all phases. [NR]

of picking approaches are possible. We follow (Molyneux and Schmitt, 1999) but use the total signal amplitude as the objective function in order to be able to follow a specific polarity. Specifically, we follow the negative amplitudes (black in Figure 3). After the picks have been established, we detect the nearest earlier zero-crossing (change from positive to negative value) and adjust the picks to that sample, as we found it more stable. Picks at noisy trace locations are linearly interpolated with their nearest neighbors and all picks are subsequently smoothed using a 50 m moving average window. In Figure 4, we show the first break picking results for the P-wave arrivals. They are shown in blue in (a) and (b), overlaying recorded data. Then, data are shifted according to picked times. We will refer to this type of correction as a moveout correction because after it is applied recorded events should have no moveout. It can be applied in either time or temporal frequency domain. If the time domain is chosen, proper interpolation is required. However, it is better to apply it in the frequency domain. We then use zero-padded traces to avoid cyclic wraparounds. Here, we apply this moveout correction for P-waves. In (c), the moveout-corrected first arrivals appear as flat, and picking seems to be reliable. For (d), the last 20 m are misaligned with the rest of the record. However, we do not analyze velocities in those areas as they are too close to the fibers edges and cannot be properly smoothed. It is also interesting to observe that after moveout correction, P-coda events in both (c) and (d) seem well aligned. However, they maintain a slight misalignment when compared to the first arrivals. This indicates that they have propagation velocities similar to first P-wave arrivals but reach the array in a slightly different angle of incidence. This may be explained by small differences in propagation path from source to receiver array, but this statement cannot be validated.

S-wave picking is more challenging than P-waves due to several factors. First, for vertical or near-vertical earthquakes, the fiber sensitivity to S-waves is greatly diminished. As DAS measures strain along the fiber, an S-wave propagating parallel to the array should not, in theory, be recorded, as all particle motion is in perpendicular directions. Due to the complex well structure, including the casing, cement, steel tube, fiber coupling, etc., S-waves are still visible, albeit possibly in lower quality. Secondly, the direct S-waves that we aim to pick undergo severe interference with other phases in play: P coda, SP mode conversions, free surface reflections of earlier phases, etc. Finally, the fact that there is no clear silence period preceding them can pose a difficulty for many picking algorithms. In order to cope with these challenges, pre-processing is applied to S-waves records. The different stages are summarized in Figure 5. The S-phase of the $M = 1.33$ earthquake is shown in (a). We apply a moveout correction based on P-wave picking, the result of which is shown in (b). This record can now be easily filtered in the f-k domain. We design a filter that allows only for upgoing events, with a velocity lower than 11 km/s. After moveout correction, P-events have an infinite (or near-infinite) velocity and are thus filtered out. Free surface reflections are down-going and thus filtered out as well. We also limit our processing to a 10-80 Hz frequency range. Data after applying f-k filtering are shown in (c). Despite some residual interferences, the S-phase is easier to follow. In order to facilitate automatic picking, we apply another moveout correction, this

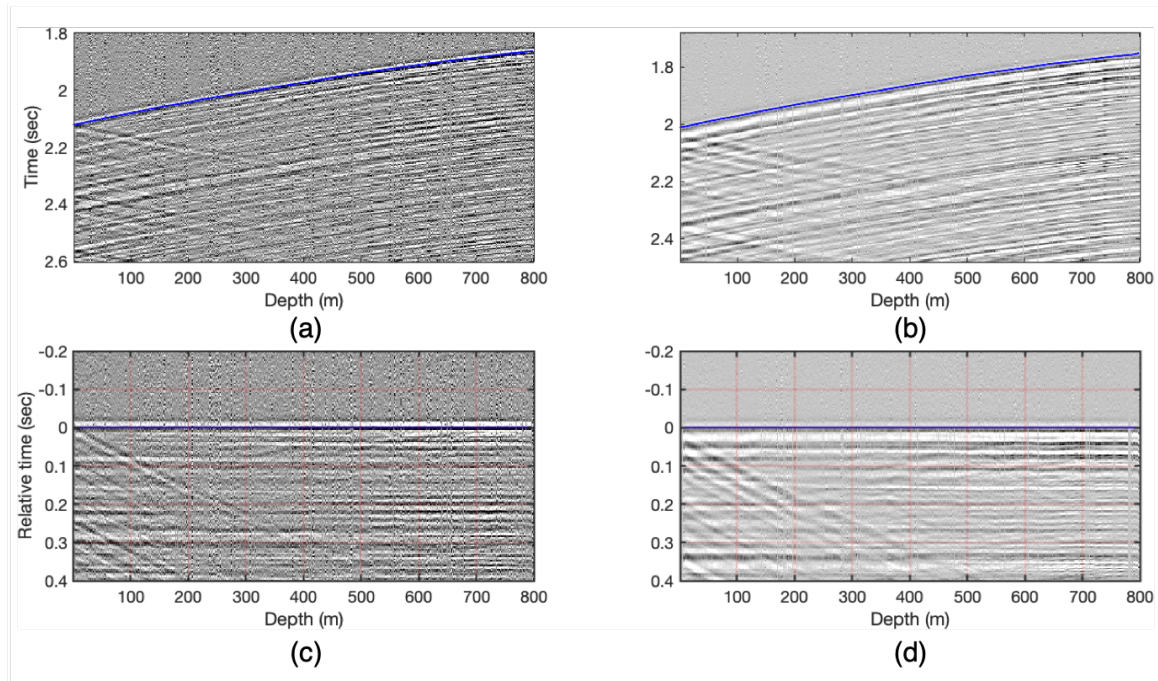


Figure 4: P-wave arrivals and their picking for both earthquakes. (a) and (b) are zoomed-in versions of Figure 3. First-break picking is overlaid in blue, indicating the zero crossing between positive (white) and negative (black) phases. In (c) and (d) we show the same records after a moveout correction based on picked times. The zero relative time is shown in blue. For the event at (d), the 780 - 800 m range seems problematic. However, this area is not used for analysis as it is too close to the edge of the array. [NR]

time with an approximated S-velocity. We assume $V_p/V_s = 1.9$ and compute the expected moveout for S-waves. Since a P-moveout was previously applied, we use the residual moveout, computed by S-P, for the second moveout correction. After doing so (d), the record is significantly flatter, especially in the deeper part of the array. It is then picked automatically, following the negative (black) phase. Picks after necessary manual editing are overlaid in red. Finally, the same picks are overlaid on the filtered but with unshifted moveout data (e). Picks seem to consistently follow the same arrival phase. However, there seems to be clear interference with other seismic phases, causing picking errors. Such errors are expected to yield noisy velocity models. Despite these limitations, it would have been more challenging to pick directly on the recorded data, probably inducing much larger errors. Estimated velocity models for both P and S phases are shown in Figure 9.

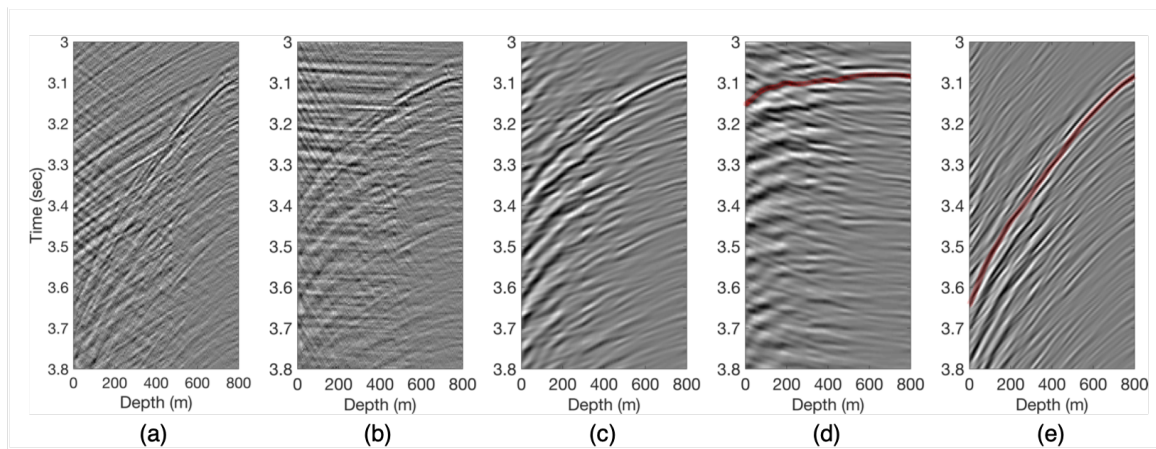


Figure 5: S wave processing. (a) Recorded S-phases for the magnitude $M=1.33$ earthquakes. (b) Record after moveout correction for P-waves. (c) Moveout-corrected record after f-k filtering. (d) Approximate correction for S-velocity and results of picking (in red). (e) Same picks overlaid on the filtered, unshifted data. Moveout-based filtering greatly simplifies the picking task. [NR]

Estimating velocity by local slant-stacks

Travel-time picking suffers from inherent limitations (Lellouch and Reshef, 2019). First, it is conducted channel-by-channel, which dictates a low signal-to-noise ratio. This is especially problematic in DAS records, in which individual channels are often noisier than conventional clamped receivers (Daley et al., 2016). In addition, picking often has to be manually guided and adjusted, which is time-consuming, error-prone, and can be hard to reproduce. Therefore, we suggest an alternative approach, which is based on local slant-stack decomposition (Biondi, 1992). It is an array-based processing technique, which aims at measuring data coherency along various possible linear velocities, represented by different slowness values p . The computed slowness range and discretization are chosen according to prior velocity model knowledge and resolu-

tion needs. In our examples, we scan a velocity range of 300 to 6000 m/s, computed by 30 m/s intervals. Coherency is computed within a certain channel window, which is chosen according to the recorded arrivals curvature. In other words, the window has to be small enough so that the recorded arrivals can be approximated by a linear slope. On the other hand, the resolution of the velocity estimation increases with window size. We choose this window as a truncated Gaussian $G(z)$ of 150 m width, with a maximum of 1 at the center channel and a value of $1/e^2$ at the edges of the window. We denote each window by its center channel depth w and one-sided width W . We use a windowed semblance measure (Neidell and Taner, 1971) to estimate data coherency. Semblance is measured in a time window of size $[-T, T]$. The choice of T is dictated by recorded data frequency. Mathematically, the local slant-stack S of recorded data d , ordered as *channel*, *sample*, is the following mapping:

$$S(w, p, t) = \frac{1}{[2W + 1]} \cdot \frac{\sum_{s=t+p \cdot dz \cdot z-T}^{s=t+p \cdot dz \cdot z+T} \left[\sum_{z=w-W}^{w+W} G(z) d(z, s) \right]^2}{\sum_{s=t+p \cdot dz \cdot z-T}^{s=t+p \cdot dz \cdot z+T} \sum_{z=w-W}^{w+W} G(z)^2 d(z, s)^2} \quad (4)$$

in which p is the slowness, and t is the event origin time. In Figure 6, we show slant-stack panels computed for three different channel windows. P-velocity events are easy to detect since they have a clear first arrival (around $t=2$ s). Many subsequent events have approximately the same velocity. About 1.25 seconds later, S-velocity phases appear. There are several events with a similar S velocity occurring at different times. However, P events are still simultaneously visible, and interference between the P and S velocities occurs. We emphasize that the slant-stack method we apply is a basic approach and more advanced methods have been successfully applied to diminish the interference between waves of different velocities (Kostov and Biondi, 1989). This might cause over-estimation of the S-wave velocities. We apply a simple procedure to automatically estimate P and S velocities. We start by estimating the P velocity. We choose the first arrivals since, from our tests, the velocity profiles estimated using them are the most stable. Therefore, we limit our analysis to a 200 ms window encapsulating all first arrivals along the array. In this window, the point of maximal coherency is chosen, indicating the local velocity at the central channel. For S-velocity estimation, a longer 600 ms window is used. In addition, within that window only velocities of up to 60% of the estimated P velocity are allowed. Without this step, the maximum semblance could represent a P-velocity event, as in Figure 6(a). We then repeat the maximal semblance choice procedure. Estimated velocity models for both P and S phases are shown in Figure 9.

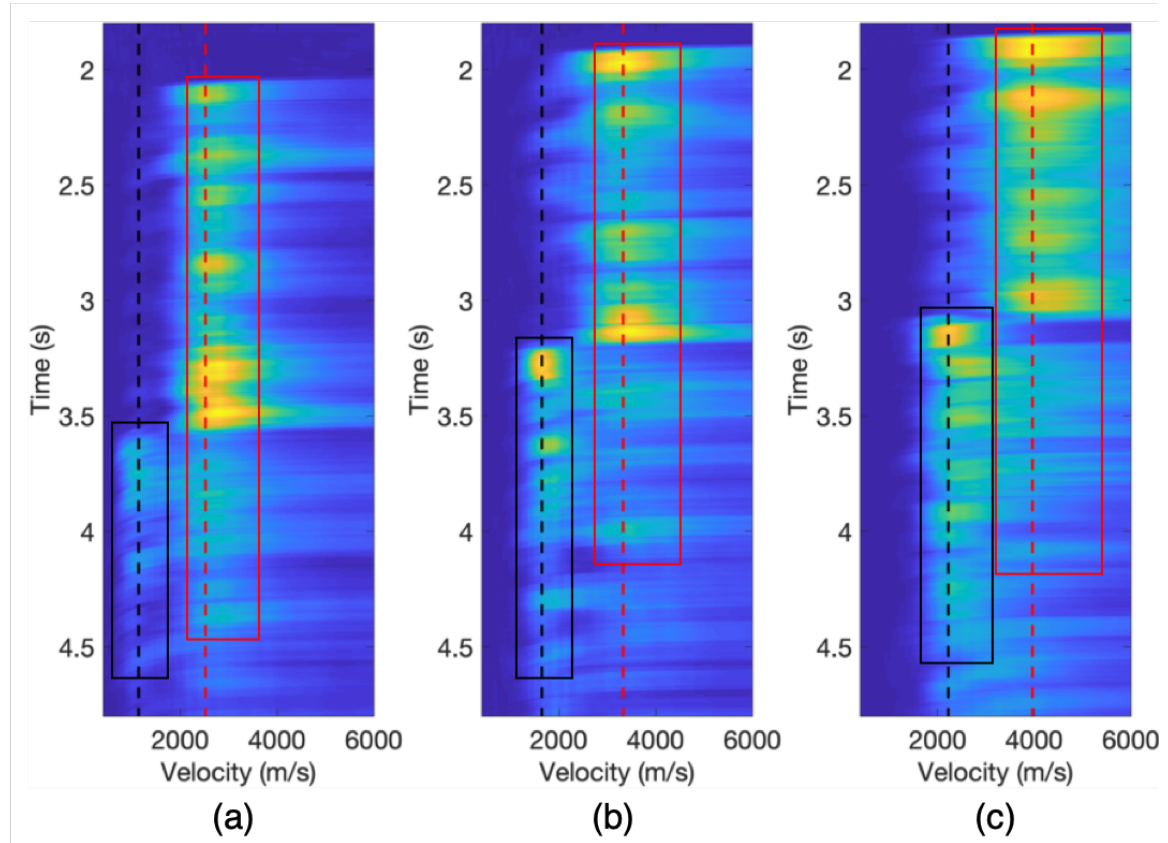


Figure 6: Slant stack panels computed for the $M = 1.33$ event at different depth locations: 0-150 m (a), 275-425 m (b) and 650-800 m (c). P-wave velocity events are approximately denoted in red boxes while S-wave velocity events are in black boxes. The automatically estimated velocities are marked by dashed lines of matching colors. For all displayed events, there is some interference between P and S events. [NR]

OTHER DOWNHOLE VELOCITY ESTIMATION METHODS

Ambient field interferometry

Retrieving surface wave response between pairs of horizontal DAS sensors using cross-correlation method (Shapiro and Campillo, 2004) has been recently shown by Zeng et al. (2017); Martin et al. (2018). Here, we show that body P-wave velocities can also be retrieved using ambient field borehole interferometry between pairs of adjacent overlying sensors (Miyazawa et al., 2008).

The ambient recorded field consists of strain (or strain rate) measurements at different depth locations. As previously discussed, the difference between strain and velocity measurements is a scaling by the velocity (Equation 3). Therefore, conventional interferometry methods, which do not take amplitude information into account, can be used directly for DAS data. The cross-correlation $C_{(A,B)}$ between two strain (ϵ) measurements at depths Z_r and Z_s is given, in the frequency domain, by:

$$C_{A,B}(\omega) = \langle \epsilon_{Z_S}(\omega) \cdot \epsilon_{Z_R}(\omega) \rangle \quad (5)$$

where $\langle \rangle$ denotes an averaging operator. The imaginary part of the Green's function \mathcal{G} between two sensors, $Im[\mathcal{G}](Z_s, Z_r)$, is inferred from the average correlation using

$$Im[\mathcal{G}] \propto \frac{\langle \epsilon_{Z_S}(\omega) \cdot \epsilon_{Z_R}(\omega) \rangle}{|S(\omega)|^2} \quad (6)$$

as in Spica et al. (2018) and where $|S(\omega)|^2$ is the power spectrum of the ambient field (Wapenaar and Fokkema, 2006). In Figure 7(a, b), we show two different possible geometries for borehole interferometry. In (a), z_s is fixed at the top channel and z_r varies along the array in 50 m increments. In (b), the distance between z_s and z_r is constant and set to 50 m. Only the ambient seismic field is used for computing cross-correlations and the influence of small earthquakes is reduced via a running-absolute-mean normalization (Bensen et al., 2007). Correlations are computed using one day of continuous data. Records are separated into 30 s windows with a 50% (15 sec) overlap. To enhance their signal-to-noise ratio, we compute correlations for nearby source-receiver pairs and stack them. These correlations are calculated using the same source channel but different receiver ones. As said before, the source channel z_s may be either fixed at the top of the array or vary along it by 50 m intervals. Stacked correlation values are, in this study, computed by $\overline{C_{S,R}} = \sum_{Z=R-10}^{R+10} C_{S,Z}$. This induces a smoothing of the velocity model but is required to extract a clear signal. Since events

within the depth range used for averaging are expected to have different time-lags, we apply travel-time shifts to the computed cross-correlation functions before stacking them. The shifts are computed using an average 3200 m/s velocity (Figure 7).

Figure 7(c, d) shows the resulting stacked correlations in the time domain after a 5-20 Hz bandpass filter. An impulsive arrival is observed on the causal side of the correlation functions. The strong signals of these down-going waves compared to the up-going ones suggest that the dominant ambient field sources originate at the surface (Zhou and Paulssen, 2017). In Figure 7(c), we observe a clear wave packet with an apparent velocity of about 3200 m/s, which corresponds to an average P-waves velocity in the vicinity of the array. Thus, we deduce we are observing a P-wave, and take the correlation functions shown in Figure 7(d) to estimate its velocity every 50 m. We estimate the arrival time by seeking the three adjacent samples with the largest values and applying quadratic interpolation to find the time at which the cross-correlation function is maximal (Nakata and Snieder, 2012). It represents the travel time for a P wave that propagates between source and average receiver location. In addition, we compute the average P-wave velocity by performing the same analysis using seven different days of recorded data. The standard deviation at different depth intervals, estimated in 50 m blocks, is between 70-90 m/s, depending on the depth of interest. The estimated P-wave velocity model is shown in Figure 9.

Conventional geophone survey

A VSP survey was conducted in April 2005 by the U.S. Geological Survey (USGS) using a downhole 3-C geophone array contributed by Paulsson Geophysical Services, Inc. Explosive sources were detonated more than 40 m away from the wellhead at a depth of about 3 m (Figure 1). We only use the vertical component of the 3-C geophones. Explosive sources in this configuration do not generate visible S-waves that can be used for velocity analysis. Therefore, we focus on P-wave model building, conducted with the vertical recording component. Data recorded for the two different explosive sources are shown in Figure 8, with overlaying picked arrivals (red). The average central frequency is about 55 Hz. It is important to remember that the shallow subsurface induces noticeable dissipation on recorded signals, leading to the relatively stronger loss of high-frequencies. Thus, even explosive sources can reach downhole receivers with a relatively low frequency content. The picking procedure that was described in the subsection *Estimating velocity by travel-time picking* is applied here, following the positive (white) phase instead. The choice of phase to pick depends on recorded signal wavelet. Picking here is unambiguous set aside one noisy trace for which the pick was interpolated. However, since sources are excited from offset, processing must be adapted. For a 1-D experiment, the interval velocity is computed by dz/dt , with dz being the depth difference between receivers and dt the difference between picked arrivals. Here, we take the 3-D Euclidean source-receiver distance D , and compute interval velocity by dD/dt instead. For near-vertical propagation, this first order correction is acceptable. A full solution would take into account true

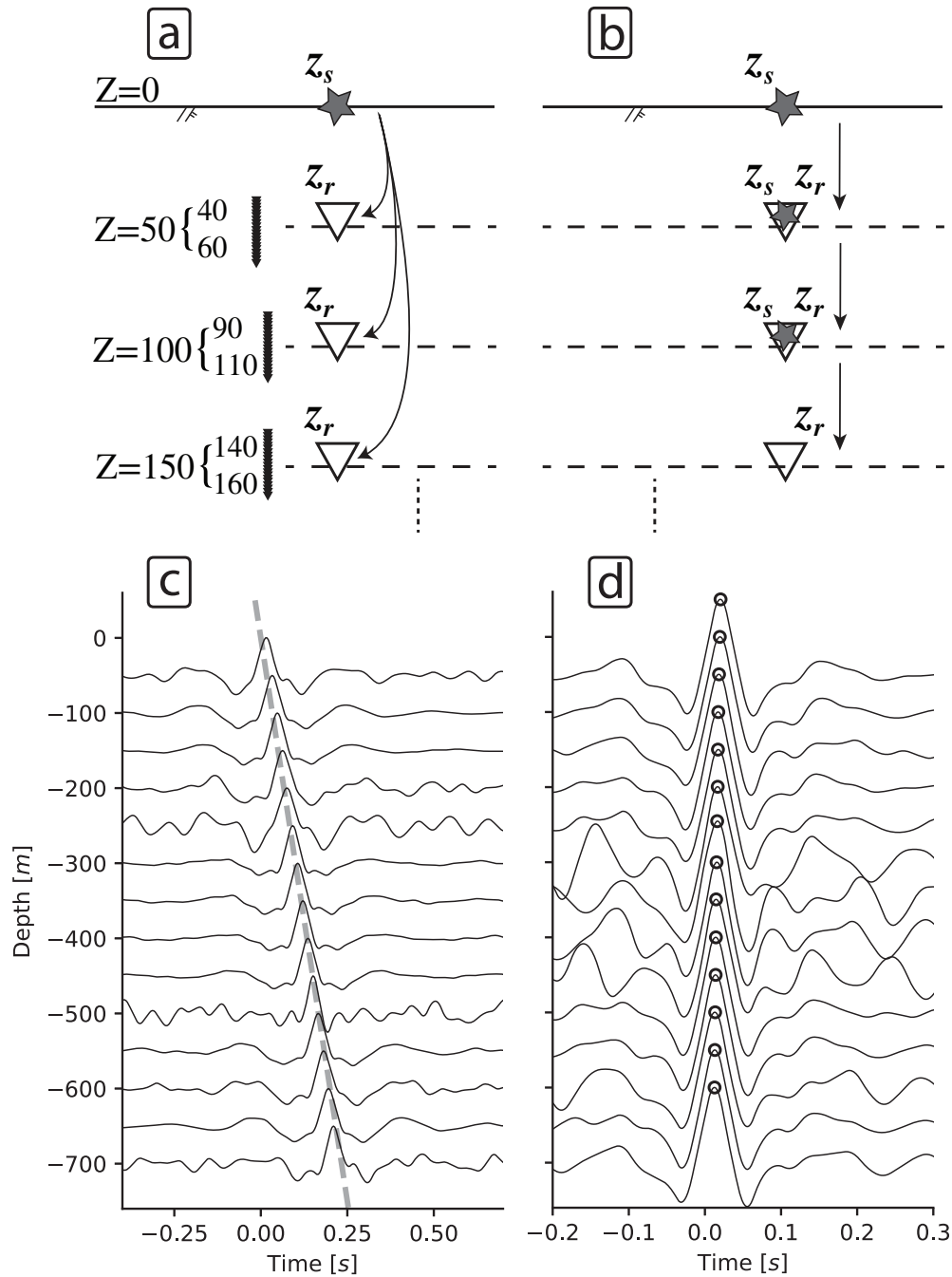


Figure 7: Two different geometries used for borehole interferometry. In (a), the source is fixed at the top channel and cross-correlations are computed with different receivers. In (b), cross-correlations are computed between source-receiver pairs of constant distance, and the same spatial locations are used as both virtual sources and receivers. In (c) and (d), we show cross-correlation results obtained with one day of data for the geometries showed in (a) and (b), respectively. In (c), the gray line depicts the average 3200 m/s P-wave velocity. In (d), the black circle depicts the picked travel times of the P-waves. [NR]

propagation paths and their differences, but it requires an initial velocity model. The estimated P-wave velocity model is shown in Figure 9.

MODELS COMPARISON AND INTERPRETATION

In this section, we summarize all extracted velocity profiles. It is important to note that picks, their difference, and the estimated velocity all require smoothing. We follow the same smoothing parameters for all datasets, and the largest operator is 100 m long. Slant-stack results were also smoothed with the same 100 m window. Results are summarized in Figure 9. There are 7 different velocity models, 5 of which are for P-wave velocity. The first two models we display are estimated using the $M = 1.33$ earthquake. They are computed using slant-stacks (solid blue) and travel-time picking (solid red), accordingly (subsections *Estimating velocity by travel-time picking* and *Estimating velocity by local slant-stacks*). We display the P model (dashed black) computed from the conventional geophone survey (subsection *Conventional geophone survey*) and the model extracted using ambient field interferometry (solid green, subsection *Ambient field interferometry*). In dotted cyan, we plot a regional P model, obtained from surface seismic surveys (Bleibinhaus et al., 2007; Hole et al., 2006). We could only obtain S-wave velocities using recorded earthquakes, and thus display the velocities estimated using slant-stack (dotted blue) and picking (dotted red), respectively. We also display the computed V_P/V_S for both slant-stack and travel-time picking analysis.

Velocity models obtained using slant-stack and travel-time picking of a recorded earthquake are very similar to the results of a conventional downhole survey processing. Quantitatively, the average difference between them is 2% for the slant-stack result and 2.7% for the picks-based result. The average difference between slant-stack and picking results is 2.1%. We thus treat those results as practically equivalent. More importantly, they all seem to have the same overall structure - velocity increase up to about 300 m, fixed or slowly increasing velocity between 300 m and 500 m, and velocity increase from 500 m and deeper. These three models follow the general trend set by the regional model but have much higher resolution. Recovering high-resolution variation in the shallow subsurface, especially in non-reflective geology, is a major challenge for surface seismic. Therefore, it is not surprising that the regional model cannot obtain the same resolution. The model estimated from ambient field interferometry is of intermediate quality between the regional model and the high-resolution models. It is closer to the latter but appears to follow a somewhat linear trend, in contrast to the high-resolution models. This result is expected as we compute the velocity model using low frequency (5-20 Hz) data. We emphasize that the interferometry analysis is relatively simple and uses one-day long data records.

The estimated S-model follows the high-resolution velocity structure of the P-model. The velocity model estimated using travel-time picking is noisier. This is due to interference with other seismic phases, as previously discussed. The V_P/V_S seems to be significantly increasing when approaching the surface. Our analysis can be safely

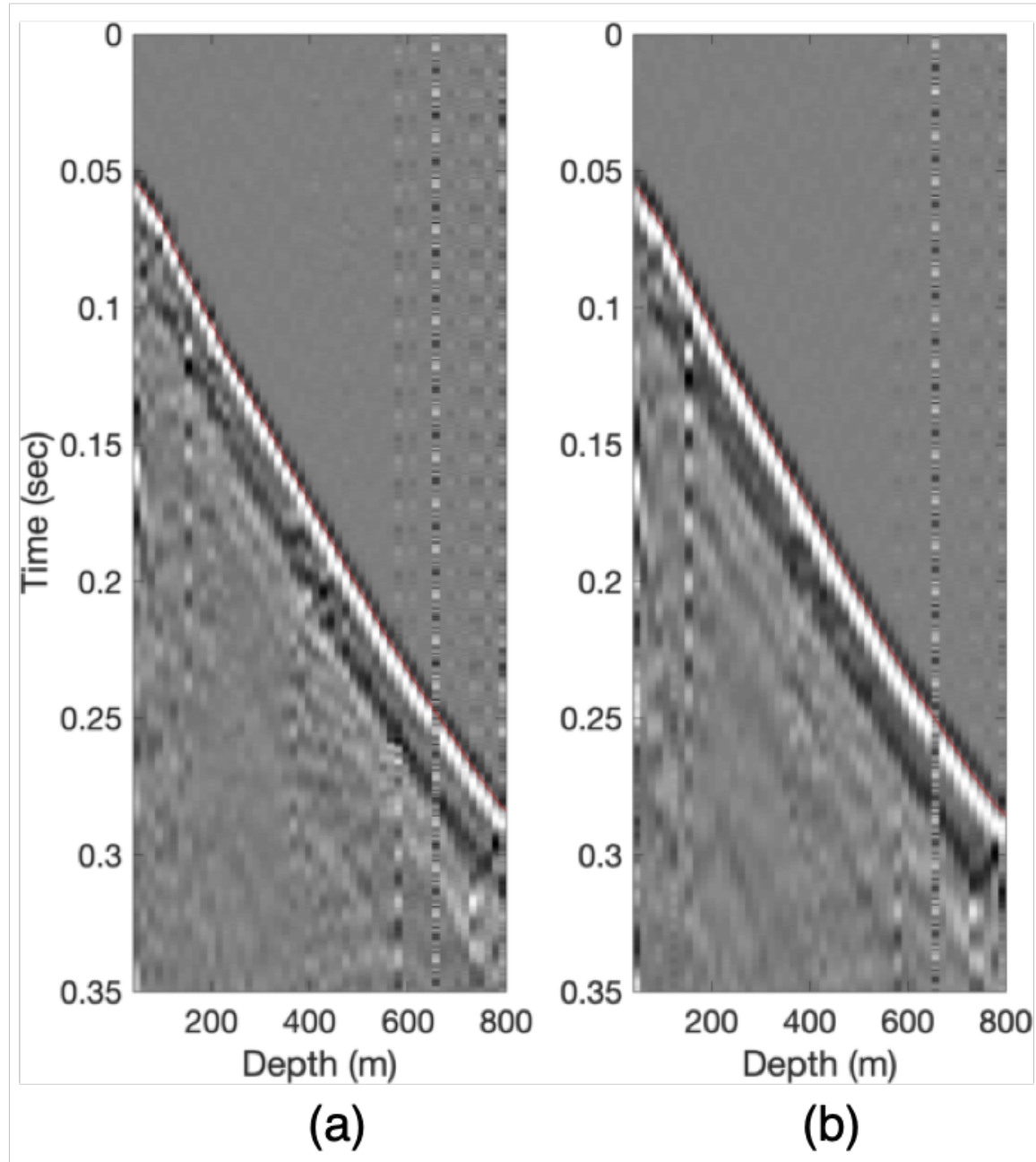


Figure 8: VSP explosive sources recorded by downhole geophones. Two different explosive sources were used 5 lb (a) and 7 lb (b). Source and receiver locations are described in Figure 1. For both sources, picking the first break arrival is easy. It is overlaid in red, following the zero crossing between negative (black) and positive (white) phases. The noisy channel at 650m is not picked and we interpolate the arrival time using nearby channels. [NR]

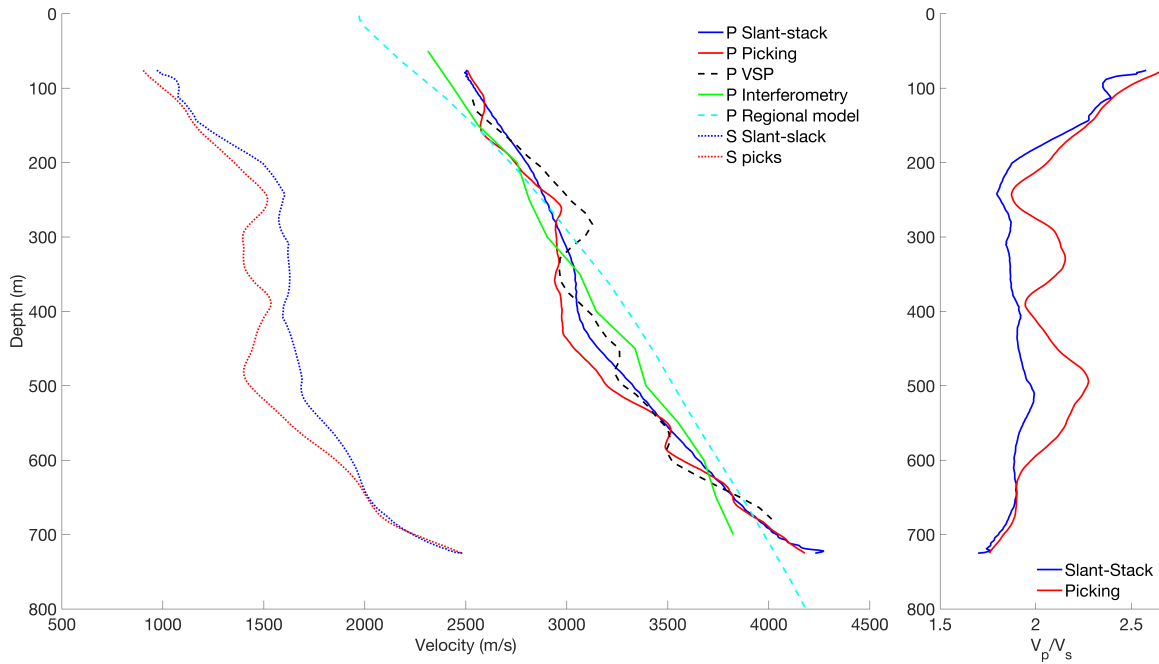


Figure 9: Estimated velocity models and V_P/V_S . We plot five P velocity models: slant-stack (blue) and travel-time picking (red) results using the $M = 1.33$ earthquake record, conventional VSP processing (black), ambient field interferometry (green), and regional model (cyan). We compute S wave velocities using the same earthquake record and display slant-stack (dotted blue) and picking-based (dotted red) results. The V_P/V_S computed using slant-stack (blue) and picking (red) results, are shown on the right. Velocity models extracted from DAS records and the VSP survey are close (2.6% average difference) and follow the regional model trend. However, they seem to reveal more geological features. The interferometry model seems to be of intermediate quality. V_P/V_S increases close to the surface using both methods. In addition, it shows a high-value anomaly at a depth of 500-520 m. This anomaly is evident from the picking-based model and noticeable in the slant-stack estimation. [NR]

conducted at depths of 75 m and deeper, but from following the trend it appears that at surface level values of $V_P/V_S = 3$ and above can be expected. As we previously show, strong interference with different phases turns the picking of the S-phase unstable. As a result, the estimated velocity model is somewhat noisy. Nonetheless, there seems to be a significant high-value anomaly of V_P/V_S around a depth of 500-520 m for both analysis methods, albeit it is more evident from the picking-based method. This could be connected to the 3-blocks model we suggest, as the 500 m depth mark seems to be a transition point between the second and third blocks. We believe we have an experimental observation confirming that V_P/V_S anomaly. In Figure 10, we show the $M = 2.46$ earthquake, with true relative amplitude values (no trace normalization). This earthquake is an independent measurement, as the V_P/V_S profile was computed without it. In a red rectangle, we highlight a specific event. It has a P-wave moveout, much like the coda P events before and possibly after it. However, the events amplitude is much stronger than the preceding coda P waves. In addition, its phase behavior (negative-positive-negative), as well as its lower frequency, distinguish it from coda P waves. Therefore, we suggest that this event is a converted SP mode, as S arrivals are much stronger. It originates roughly at the 500m depth marker, indicative of a strong P/S contrast and possible transition between structural blocks.

DISCUSSION

In this study, we show how earthquakes recorded by downhole DAS systems can be used for P- and S- wave velocity estimation along the well. A recorded $M = 1.33$ earthquake at a distance of more than 10km from the array has a central frequency of 70 Hz. It is higher than a conventional geophone survey, having about 55 Hz. In addition, geophones are positioned roughly every 15 m whereas the DAS array offers continuous (1m spacing) recording. In seismically active areas, recorded earthquakes of relatively low magnitudes can be a source of high-frequency data. In addition, such earthquakes propagate through the highly dissipative shallow subsurface last, allowing for high-frequency records along most of their propagation path. Surface sources, on the contrary, immediately suffer from dissipation, thus reducing recorded frequency content. For P-waves, models estimated using two different analysis methods are within less than 3% absolute mean difference of a much more expensive VSP geophone survey. The methodology depends on earthquakes that propagate near-vertically, but incidence angles of up to 15-20 degrees are judged acceptable. Moreover, earthquakes with higher incidence angles may be used with appropriate scaling. Slant-stack estimation of local velocity is automatic once several parameters have been chosen. These parameters are the size and shape of the spatial window, temporal window, and a minimum V_P/V_S . Travel-time picking, on the contrary, requires manual choices, quality control, and possible intervention. While for our examples, it is relatively straightforward for P-phases, this may not be the case for low signal-to-noise records. In addition, S-wave processing is challenging even with high signal-to-noise data. It is due to P-wave interference (coda waves, converted modes, free surface reflections) as

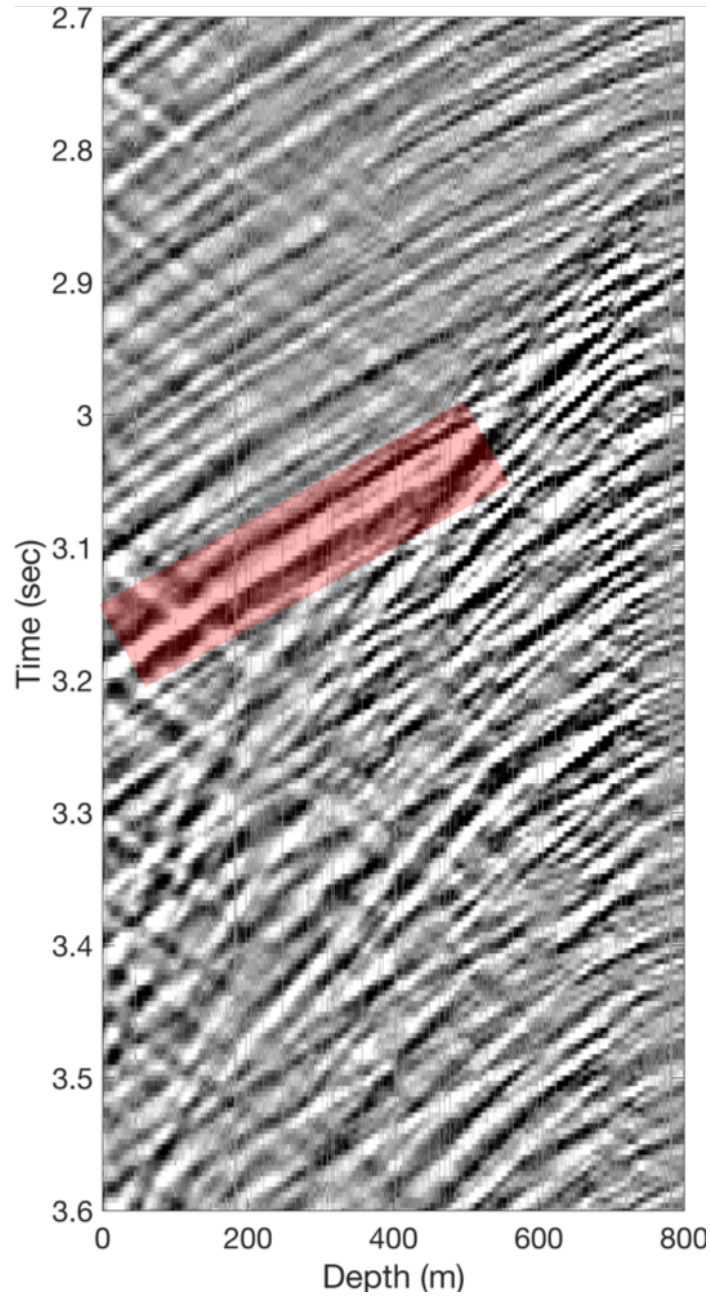


Figure 10: Highlighting of an SP converted event. We display the record with constant gain, so relative amplitudes are preserved. The converted event is highlighted by a red rectangle. It has a clear P-moveout and strong amplitudes. Therefore, it seems to originate from the strong S-phase energy. In addition, it has a lower frequency and different temporal behavior when compared to surrounding P coda waves. [NR]

well as the directivity of the fiber, which lacks sensitivity to S-phases propagating along it. Therefore, some pre-processing prior to picking is necessary. An alternative approach is to apply ambient field interferometry, which can be performed with as little as one day of continuous data. However, it does not recover S-wave velocities. Using one day of recorded data, input correlograms for P-wave velocity estimation are of significantly lower frequency content (5-20 Hz). Therefore, the retrieved P-wave model is of lower resolution. Regardless of the velocity estimation method, the advantages of array-based processing are evident. The benefits of such processing stand out when handling S-phases. Records are very complex and consist of many different phases: direct P, P coda, direct S, converted modes (SP, PS), S coda, free surface reflections of all phases, etc. Trying to analyze S arrivals using surface receivers only would be extremely challenging. Here, on the contrary, array-based filtering, based on event moveout with depth, can be applied and greatly simplify processing. It also allows for a better understanding of subsurface phenomena, like the SP converted event we show. Thanks to its continuous sampling in depth, we can be much more certain of its interpretation, and even link it to extracted velocity models. Downhole DAS analysis is especially beneficial in recovering shallow velocity structures, which often remain unresolved by conventional seismic surveys. However, it may also be a basis for different applications. For example, it can be conducted periodically to detect changes in velocity along the array. Ambient field interferometry is a natural candidate for such an application. Nonetheless, since monitoring is often conducted in seismically active areas, enough near-vertical earthquake could be present for an event-based analysis. In addition, coda waves and converted modes may be looked into more systematically to refine velocity structures, especially in defining areas of contrast.

CONCLUSIONS

The array nature of the downhole DAS allows for advanced processing techniques, clear phase separation and understanding, and higher combined signal-to-noise ratio. Downhole DAS records can be used for velocity model estimation along the array. Relatively weak recorded earthquakes have a high frequency content. Using near-vertical recorded earthquakes, P- and S- velocities are estimated using slant-stacks and travel-time picking. Obtained results match a P-wave model extracted from a conventional geophone-based VSP survey, which cannot yield an S-wave velocity model. The P-wave velocity profiles we obtain are much more detailed than a regional model estimated from surface seismic surveys. Interferometry is a useful alternative when no adequate earthquakes are recorded. However, a P-wave model computed using ambient field is superior to the regional model but not as detailed as the models extracted using recorded earthquakes. In addition, it does not yield S-wave velocities. Application of earthquake-based analysis in the top 800m of the SAFOD borehole reveals three distinct geological blocks, concealed in the regional and interferometry-based models. V_P/V_S analysis shows high values close to the surface and a high-ratio anomaly at a depth of 500 to 520 m. An SP converted mode event originating at this

depth zone confirms a geological contrast.

REFERENCES

- Ajo-Franklin, J., S. Dou, N. Lindsey, T. M. Daley, B. Freifeld, E. R. Martin, M. Robertson, and C. Ulrich, 2017, Timelapse surface wave monitoring of permafrost thaw using distributed acoustic sensing and a permanent automated seismic source: SEG Technical Program Expanded Abstracts 2017, 5223–5227.
- Armstrong, T., J. McAteer, and P. Connolly, 2001, Removal of overburden velocity anomaly effects for depth conversion: *Geophysical Prospecting*, **49**, 79–99.
- Bakulin, A., and R. Calvert, 2006, The virtual source method: Theory and case study: *Geophysics*, **71**, SI139–SI150.
- Bakulin, A., P. Golikov, R. Smith, K. Erickson, I. Silvestrov, and M. Al-Ali, 2017, Smart DAS upholes for simultaneous land near-surface characterization and sub-surface imaging: *The Leading Edge*, **36**, 1001–1008.
- Bensen, G. D., M. H. Ritzwoller, M. P. Barmin, A. L. Levshin, F. Lin, M. P. Moschetti, N. M. Shapiro, and Y. Yang, 2007, Processing seismic ambient noise data to obtain reliable broad-band surface wave dispersion measurements: *Geophysical Journal International*, **169**, 1239–1260.
- Biondi, B., 1992, Velocity Estimation by Beam Stack: *Geophysics*, **57**, 1034–1047.
- Biondi, B., E. Martin, S. Cole, M. Karrenbach, and N. Lindsey, 2017, Earthquakes analysis using data recorded by the Stanford DAS Array: SEG Technical Program Expanded Abstracts, 2752–2756.
- Bleibinhaus, F., J. A. Hole, T. Ryberg, and G. S. Fuis, 2007, Structure of the California Coast Ranges and San Andreas Fault at SAFOD from seismic waveform inversion and reflection imaging: *Journal of Geophysical Research: Solid Earth*, **112**, B06315.
- Blias, E., 2009, Stacking velocities in the presence of overburden velocity anomalies: *Geophysical Prospecting*, **57**, 323–341.
- Blum, J. A., S. L. Nooner, and M. A. Zumberge, 2008, Recording earth strain with optical fibers: *IEEE Sensors Journal*, **8**, 1152–1160.
- Daley, T. M., B. M. Freifeld, B. Ajo-Franklin, S. Dou, R. Pevzner, S. Shulakova, Valeriya Kashikar, D. E. Miller, J. Goetz, J. Henniges, and S. Lueth, 2013, Field testing of fiber-optic distributed acoustic sensing (DAS) for subsurface seismic monitoring: *The Leading Edge*, **32**, 699–706.
- Daley, T. M., D. E. Miller, K. Dodds, P. Cook, and B. M. Freifeld, 2016, Field testing of modular borehole monitoring with simultaneous distributed acoustic sensing and geophone vertical seismic profiles at Citronelle, Alabama: *Geophysical Prospecting*, **64**, 1318–1334.
- Dean, T., T. Cuny, and A. H. Hartog, 2017, The effect of gauge length on axially incident P-waves measured using fibre optic distributed vibration sensing: *Geophysical Prospecting*, **65**, 184–193.
- Dou, S., N. Lindsey, A. M. Wagner, T. M. Daley, B. Freifeld, M. Robertson, J. Peterson, C. Ulrich, E. R. Martin, and J. B. Ajo-Franklin, 2017, Distributed Acoustic

- Sensing for Seismic Monitoring of the Near Surface: A Traffic-Noise Interferometry Case Study: *Scientific Reports*, **7**, 1–12.
- Grattan, L., and B. Meggitt, 2000, *Optical fiber sensor technology: Fundamentals*, springer ed.: Springer.
- Hardage, B. A., 2000, *Vertical seismic profiling : Principles*, 3rd ed.: Elsevier Science.
- Hole, J. A., T. Ryberg, G. S. Fuis, F. Bleibinhaus, and A. K. Sharma, 2006, Structure of the San Andreas fault zone at SAFOD from a seismic refraction survey: *Geophysical Research Letters*, **33**, L07312.
- Hornman, J. C., 2017, Field trial of seismic recording using distributed acoustic sensing with broadside sensitive fibre-optic cables: *Geophysical Prospecting*, **65**, 35–46.
- Jousset, P., T. Reinsch, T. Ryberg, H. Blanck, A. Clarke, R. Aghayev, G. P. Hersir, J. Hennings, M. Weber, and C. M. Krawczyk, 2018, Dynamic strain determination using fibre-optic cables allows imaging of seismological and structural features: *Nature Communications*, **9**, 2509–2519.
- Karrenbach, M., D. Kahn, S. Cole, A. Ridge, K. Boone, J. Rich, K. Silver, and D. Langton, 2017, Hydraulic-fracturing-induced strain and microseismic using in situ distributed fiber-optic sensing: *The Leading Edge*, **36**, 837–844.
- Kostov, C., and B. Biondi, 1989, High-Resolution Velocity Spectra Using Eigenstructure Methods: *Geophysics*, **54**, 832–842.
- Landrø, M., 1999, Repeatability issues of 3-D VSP data: *Geophysics*, **64**, 1673–1679.
- Lellouch, A., and M. Reshef, 2019, Velocity analysis and subsurface source location improvement using moveout-corrected gathers: *Geophysics*, **84**, 1–59.
- Lindsey, N. J., E. R. Martin, D. S. Dreger, B. Freifeld, S. Cole, S. R. James, B. L. Biondi, and J. B. Ajo-Franklin, 2017, Fiber-Optic Network Observations of Earthquake Wavefields: *Geophysical Research Letters*, **44**, 792–799.
- Madsen, K. N., R. Tøndel, and Ø. Kvam, 2016, Data-driven depth calibration for distributed acoustic sensing: *The Leading Edge*, **35**, 610–614.
- Martin, E., B. Biondi, M. Karrenbach, and S. Cole, 2017a, Ambient Noise Interferometry from DAS Array in Underground Telecommunications Conduits: Presented at the 79th EAGE Conference & Exhibition.
- Martin, E. R., and B. L. Biondi, 2018, Eighteen Months of Continuous Near-surface Monitoring with DAS Data Collected Under Stanford University: *SEG Technical Program Expanded Abstracts 2018*, 4958–4962.
- Martin, E. R., C. M. Castillo, S. Cole, P. S. Sawasdee, S. Yuan, R. Clapp, M. Karrenbach, and B. L. Biondi, 2017b, Seismic monitoring leveraging existing telecom infrastructure at the SDASA : Active , passive , and ambient-noise analysis: *The Leading Edge*, **36**, 1025–1031.
- Martin, E. R., N. J. Lindsey, and B. Biondi, 2018, Introduction to Interferometry of Fiber Optic Strain Measurements: *EarthArXiv*, **14 June**, 1–33.
- Mateeva, A., J. Lopez, J. Mestayer, P. Wills, B. Cox, D. Kiyashchenko, Z. Yang, W. Berlang, R. Detomo, and S. Grandi, 2013, Distributed acoustic sensing for reservoir monitoring with VSP: *The Leading Edge*, **32**, 3–7.
- Mateeva, A., J. Lopez, H. Potters, J. Mestayer, B. Cox, D. Kiyashchenko, P. Wills, S. Grandi, K. Hornman, B. Kuvshinov, W. Berlang, Z. Yang, and R. Detomo, 2014, Distributed acoustic sensing for reservoir monitoring with vertical seismic profiling:

- Geophysical Prospecting, **62**, 679–692.
- Miyazawa, M., R. Snieder, and A. Venkataraman, 2008, Application of seismic interferometry to extract P- and S-wave propagation and observation of shear-wave splitting from noise data at Cold Lake, Alberta, Canada: *Geophysics*, **73**, D35–D40.
- Molyneux, J. B., and D. R. Schmitt, 1999, First-break timing : Arrival onset times by direct correlation: *Geophysics*, **64**, 1492–1501.
- Nakata, N., and R. Snieder, 2012, Estimating near-surface shear wave velocities in Japan by applying seismic interferometry to KiK-net data: *Journal of Geophysical Research: Solid Earth*, **117**, 1–13.
- Neidell, N. S., and M. T. Taner, 1971, Semblance and Other Coherency Measures for Multichannel Data: *Geophysics*, **36**, 482–497.
- Nosjean, N., F. Hanot, J. P. Gruffeille, and F. Miquelis, 2017, Statics : from imaging to interpretation pitfalls and an efficient way to overcome them: *First Break*, **35**, 71–78.
- Parker, T., S. Shatalin, and M. Farhadiroushan, 2014, Distributed Acoustic Sensing - A new tool for seismic applications: *First Break*, **32**, 61–69.
- Shapiro, N. M., and M. Campillo, 2004, Emergence of broadband Rayleigh waves from correlations of the ambient seismic noise: *Geophysical Research Letters*, **31**, 8–11.
- Spica, Z. J., M. Perton, N. Nakata, X. Liu, and G. C. Beroza, 2018, Site characterization at Groningen gas field area through joint surface-borehole H/V analysis: *Geophysical Journal International*, **212**, 412–421.
- Waldhauser, F., and W. L. Ellsworth, 2000, A Double-difference Earthquake location algorithm: Method and application to the Northern Hayward Fault, California: *Bulletin of the Seismological Society of America*, **90**, 1353–1368.
- Wang, H. F., X. Zeng, D. E. Miller, D. Fratta, K. L. Feigl, C. H. Thurber, and R. J. Mellors, 2018, Ground motion response to an ML 4.3 earthquake using collocated distributed acoustic sensing and seismometer arrays: *Geophysical Journal International*, **213**, 2020–2036.
- Wapenaar, K., and J. Fokkema, 2006, Green’s function representations for seismic interferometry: *Geophysics*, **71**, SI33–SI46.
- Zeng, X., C. Lancelle, C. Thurber, D. Fratta, H. Wang, N. Lord, A. Chalari, and A. Clarke, 2017, Properties of noise cross-correlation functions obtained from a distributed acoustic sensing array at Garner Valley, California: *Bulletin of the Seismological Society of America*, **107**, 603–610.
- Zhou, W., and H. Paulssen, 2017, P and S Velocity Structure in the Groningen Gas Reservoir From Noise Interferometry: *Geophysical Research Letters*, **44**, 11,785–11,791.
- Zoback, M., S. Hickman, and W. Ellsworth, 2011, Scientific drilling into the San Andreas fault zone - An overview of SAFOD’s first five years: *Scientific Drilling*, **22**, 14–28.